RESEARCH ARTICLE SUMMARY

GAS GIANT PLANETS

The low-frequency source of Saturn's kilometric radiation

L. Lamy*, P. Zarka, B. Cecconi, R. Prangé, W. S. Kurth, G. Hospodarsky, A. Persoon, M. Morooka, J.-E. Wahlund, G. J. Hunt

INTRODUCTION: Planetary auroral radio emissions are powerful nonthermal cyclotron radiation produced by magnetized planets. Their remote observation provides information on planetary auroral processes and magnetospheric dynamics. Understanding how they are generated requires in situ measurements from within their source region. During its early 2008 high-inclination orbits, the Cassini spacecraft unexpectedly sampled two local sources of Saturn's kilometric radiation (SKR) at 10-kHz frequencies, corresponding to the low-frequency (LF) portion of its 1- to 1000-kHz typical spectrum (hence only observable from space). These provided insights into the underlying physical excitation mechanism. The combined analysis of radio, plasma, and magnetic field in situ measurements demonstrated that the cyclotron maser instability (CMI), which generates auroral kilometric radiation (AKR) at Earth, is a universal generation mechanism able to operate in widely different planetary plasma environments. The CMI requires accelerated (out-of-equilibrium) electrons and low-density magnetized plasma, such as auroral regions where the ratio of the electron plasma frequency f_{pe} to the electron cyclotron frequency f_{ce} is much lower than unity.

RATIONALE: Intensifications of the SKR spectrum in general, and of its LF part in particular, have been widely used as a diagnostic of Saturn's large-scale magnetospheric dynamics, such as the SKR rotational modulation or major auroral storms driven by the solar wind. However, the limited set of events encountered in 2008 did not provide a comprehensive picture of the source of SKR LF emissions and of the conditions in which the CMI can trigger them.

During the 20 ring-grazing high-inclination orbits and the preceding 7 orbits, which together spanned late 2016 to early 2017, the Cassini spacecraft repeatedly sampled the top of the SKR emission region, at distances of a few planetary radii (R_S), corresponding to the lowest-frequency part of the SKR spectrum. SKR emission frequency is close to f_{ce}, itself proportional to the magnetic field amplitude, and so decreases with increasing distance from the planet. We conducted a survey of these orbits to extract the average properties of the radio sources encountered and assess the ambient magnetospheric plasma parameters that control them.

RESULTS: Throughout this set of trajectories, we were able to identify only three SKR sources. They covered the 10- to 20-kHz range (3.5 to 4.5 R_S distances from the planet's center) and were solely found on the northern dawn-side sector. The source regions hosted narrow-banded emission, propagating in the extraordinary wave mode, and radiated quasi-perpendicularly to the magnetic field lines. Their emission frequency, measured in situ, was fully consistent with the CMI mechanism driven by 6- to 12-keV electron beams with shell-type velocity distribution functions, as for AKR at Earth.

The SKR sources were embedded within larger regions of upward currents, themselves coincident with the ultraviolet (UV) auroral oval, which was observed simultaneously with the Hubble Space Telescope. However, unlike the terrestrial case, the spacecraft exited the radio source region before exiting the main oval, itself strictly coincident with the upward current layer, when the ratio f_{pe}/f_{ce} exceeded the typical CMI threshold of 0.1. This occurred at times of sudden local increases of the magnetospheric electron density.

CONCLUSION: The generation conditions of SKR LF emission appear to be strongly time-variable. The SKR spectrum additionally displays a significant local time dependence, with the lowest frequencies (the highest altitudes) reached for dawn-side radio sources. The characteristics of CMI-unstable electrons at 3.5 to 4.5 R_S imply that downward electron acceleration took place at farther distances along the auroral magnetic field lines and brings new constraints to particle acceleration models. Finally, the LF SKR component is mainly controlled by local plasma conditions, namely time-variable magnetospheric electron densities, which can quench the CMI mechanism even if accelerated electrons are present. This explains why the magnetic field lines hosting SKR LF sources can map to a restricted portion of the UV auroral oval and associated upward current region. ∎

Schematic view of Saturn's auroral emissions.
Auroral radio emissions observed above the atmosphere were remotely mapped from Cassini (the most intense emissions in red) when the spacecraft encountered a low-frequency radio source. The magnetic field lines hosting it, sampled in situ by the probe, map to the (atmospheric) UV auroral oval, as observed simultaneously by the Hubble Space Telescope.
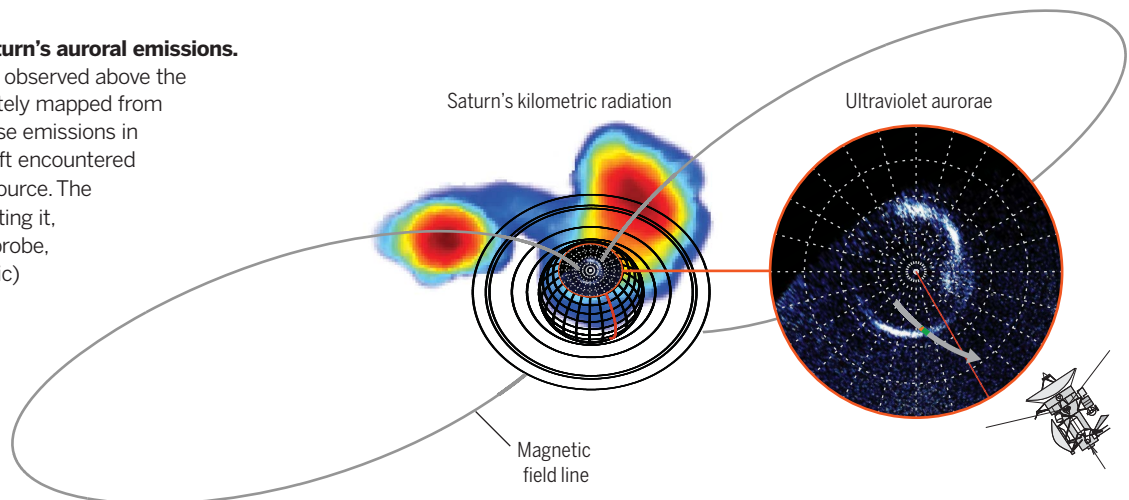
Saturn's kilometric radiation

Ultraviolet aurorae

Magnetic field line

RESEARCH ARTICLE

The low-frequency source of Saturn's kilometric radiation

L. Lamy[1]*, P. Zarka[1], B. Cecconi[1], R. Prangé[1], W. S. Kurth[2], G. Hospodarsky[2], A. Persoon[2], M. Morooka[3], J.-E. Wahlund[3], G. J. Hunt[4]

Understanding how auroral radio emissions are produced by magnetized bodies requires in situ measurements within their source region. Saturn's kilometric radiation (SKR) has been widely used as a remote proxy of Saturn's magnetosphere. We present wave and plasma measurements from the Cassini spacecraft during its ring-grazing high-inclination orbits, which passed three times through the high-altitude SKR emission region. Northern dawn-side, narrow-banded radio sources were encountered at frequencies of 10 to 20 kilohertz, within regions of upward currents mapping to the ultraviolet auroral oval. The kilometric waves were produced on the extraordinary mode by the cyclotron maser instability from 6– to 12–kilo–electron volt electron beams and radiated quasi-perpendicularly to the auroral magnetic field lines. The SKR low-frequency sources appear to be strongly controlled by time-variable magnetospheric electron densities.

Saturn is a powerful planetary radio emitter, dominated in intensity by Saturn's kilometric radiation (SKR). This nonthermal auroral emission, equivalent to auroral kilometric radiation (AKR) at Earth, is produced at frequencies f close to the local electron cyclotron frequency f_{ce}, itself proportional to the magnetic field amplitude and thus decreasing with increasing distances from the planet. The SKR spectrum ranges from a few kHz to 1 MHz (thus only observable from space), which corresponds to radio sources distributed along auroral field lines from slightly above the ionosphere up to several planetary radii R_S (1 R_S = 60,268 km is Saturn's radius). Remote observations of SKR have long been used as a proxy of kronian auroral processes and magnetospheric dynamics (1).

During its early 2008 high-inclination passes, the Cassini spacecraft unexpectedly encountered two SKR low-frequency (LF) source regions. The combined analysis of radio, plasma, and magnetic field in situ measurements showed that the cyclotron maser instability (CMI), which generates AKR at Earth, also produces SKR at Saturn, suggesting a universal process able to operate in widely different planetary magnetospheres. The CMI is a wave-electron resonant interaction that requires (i) accelerated (out-of-equilibrium) weakly relativistic electrons, whose velocity distribution function displays a positive gradient along the velocity direction perpendicular to the magnetic field, and (ii) an electron plasma frequency f_{pe} much lower than f_{ce} (2). When these two conditions are fulfilled, radio emission is amplified, mainly on the right-hand extraordinary (R-X) wave propagation mode, at the frequency $f_{CMI} = f_{ce}/\Gamma + k_\parallel v_\parallel/2\pi$ where k is the wave vector, v the electron velocity, the $\parallel$ subscript refers to the direction parallel to the magnetic field and $\Gamma = 1/\sqrt{1-v^2/c^2}$ is the Lorentz factor (3). Waves are thus amplified at the local relativistic electron cyclotron frequency, Doppler-shifted by the parallel propagation. To first order, this expression approximates to $f_{CMI} \sim f_{ce}$.

A first SKR source was identified on day 2008-291 (17 October) at 10 kHz (corresponding to 5 R_S distance from Saturn's center), at the unexpected Local Time (LT) of 01:00 and along magnetic field lines with −80° invariant latitude. Source traversal occurred during a global SKR intensification extending to low frequencies with wave electric fields of a few mV m^{-1}. It coincided with strong upward-directed field-aligned currents, indicating down-going electron beams, triggered by a major solar wind–driven compression of the magnetosphere (4–6). The R-X mode source was identified from measurements of its low-frequency cutoff f_{SKR} at about 2% below f_{ce}. Radio waves displayed strong linear polarization at the source from which they were radiated quasi-perpendicularly to the local magnetic field. In this case, f_{SKR} can be expressed as $f_{CMI} = f_{ce}\sqrt{1-v^2/c^2}$ and direct measurements of f_{SKR} yielded CMI-resonant electrons of 6 to 9 keV, in agreement with the hot (accelerated) electrons simultaneously measured in situ. Their shell-like three-dimensional (3D) distribution function (referred to as horseshoe in 2D) was

also fully consistent with CMI-driven perpendicular emission. Sampling down-going electrons with shell-like distribution implies that they had been accelerated toward the planet in regions located farther than the radio source along the flux tube (4, 7–9). A second direct confirmation of the CMI mechanism was brought by the agreement between the wave properties observed within the source region and the simulated CMI wave growth rate and emission angle driven by the electron distribution function, measured simultaneously (9). As at Earth, the auroral plasma surrounding the emission region was hot, with a marginal cold component, and tenuous with $f_{pe}/f_{ce} \sim 0.1$ (10). Conversely, terrestrial-like plasma cavities were not observed within the radio source at the 2-s resolution of Cassini's electron measurements. This difference, together with the presence of SKR sources at larger distances from the planet than AKR sources at Earth, was attributed to the faster rotation of Saturn's magnetosphere. This means that CMI condition (ii) is generally fulfilled at high latitudes without needing small-scale cavities.

A second SKR source was likely traversed on day 2008-073 (13 March) at 5 kHz (i.e., 6 R_S distance) (11). The LF emission tangentially approached the f_{ce} curve on the corresponding dynamic spectrum (time-frequency map of wave flux density) at a more usual location, near 07:30 LT, close to the SKR peak intensity region (12), and along magnetic field lines with −77° invariant latitude. The f_{pe}/f_{ce} ratio was as low as 0.05, again fulfilling CMI condition (ii). The low-frequency cutoff f_{SKR} was not accurately measured, but 7-keV electrons with a shell-like distribution function yielded CMI wave growth rates compatible with the observed SKR R-X mode flux densities (13).

This limited set of events did not provide a comprehensive view of SKR LF sources and of the conditions under which the CMI can trigger them. Intensifications of SKR spectrum in general, and of its LF component in particular, have nevertheless long been used as a sensitive diagnostic of large-scale magnetospheric dynamics, including the SKR dual rotational modulation or auroral storms induced (or not) by the solar wind (14–25). The final high-inclination phase of the Cassini mission carried the spacecraft to high latitudes at low altitudes, providing the opportunity to statistically investigate SKR sources in situ. Those orbits began with the ring-grazing orbital sequence, during which the spacecraft repeatedly sampled the top of both northern and southern SKR emission regions, at distances corresponding to the SKR lowest frequencies. We present a survey of these orbits, extract the average properties of the radio sources encountered, and discuss the magnetospheric parameters that control them.

Survey of ring-grazing orbits

Cassini's 20 ring-grazing orbits (numbered 251 to 270), whose periapsis was outside the F-ring, were executed between days 2016-335 (30 November) and 2017-112 (22 April). They

[1]Laboratoire d'Etudes Spatiales et d'Instrumentation en Astrophysique, Observatoire de Paris, Université Paris Sciences et Lettres, Centre National de la Recherche Scientifique, Sorbonne Université, Université Paris Diderot, Sorbonne Paris Cité, 5 Place Jules Janssen, 92195 Meudon, France. [2]Department of Physics and Astronomy, University of Iowa, Iowa City, IA 52242, USA. [3]Swedish Institute of Space Physics, Box 537, SE-751 21 Uppsala, Sweden. [4]Blackett Laboratory, Imperial College London, London SW7 2BW, UK.
*Corresponding author. Email: laurent.lamy@obspm.fr

passed through auroral field lines expected to host SKR sources up to 30 kHz (40 kHz) in the dawn-side northern (dusk-side southern) hemisphere (fig. S1). They were preceded by seven orbits (numbered 244 to 250) starting on day 2016-270 (26 September) that brought the spacecraft to high latitudes and at distances close enough to the planet to probe SKR sources at a few kHz. We conducted a survey of kilometric sources encountered during these 27 orbits using combined observations of the Radio and Plasma Wave Science (RPWS) experiment (26) and the magnetometer (MAG) (27).

After the Cassini Plasma Spectrometer (CAPS) (28) ceased operating in 2012, it was no longer possible to measure in situ low-energy electron distribution functions. This prevented the identification of SKR sources from the direct analysis of simultaneous radio and electron measurements based on growth rate calculation. Instead, on the basis of the reference event of day 2008-291, SKR sources were identified solely from RPWS-HFR (high-frequency receiver) and MAG data whenever (j) the emission LF cutoff f_{SKR} passed strictly below f_{ce} and (jj) persisted for at least two consecutive RPWS-HFR measurements, obtained at a 16-s temporal resolution. Criterion (j) rests upon the assumption of perpendicular emission (examined below). Criterion (jj) conservatively avoids false detections induced by spiky signals (see examples in fig. S2). The method used to determine f_{SKR} is reminded in (2). Our survey revealed only three events that unambiguously fulfilled both criteria. They all occurred in the northern hemisphere on days 2016-339 (4 December), 2016-346 (11 December), and 2017-066 (7 March), hereafter referred to as events S_1, S_2, and S_3. No source was found in the southern hemisphere. We rejected several candidate northern SKR sources that fulfilled criterion (j) but not (jj). These may be either nearby sources (close to but not crossed by Cassini), crossings of small-sized sources lasting less than 16 s (~200 to 300 km for typical spacecraft velocity), and/or emission produced at $f_{CMI} > f_{ce}$. The latter case is possible for oblique emission, where the $k_\parallel v_\parallel$ term in the expression of f_{CMI} becomes non-negligible (8, 9).

Events S_1, S_2, and S_3 were sampled during intervals of relatively quiet solar wind activity (29). S_1 and S_2 additionally occurred close to the predicted timing of periodic northern SKR bursts, whereas event S_3 was instead in anti-phase with it (1, 22). The first two events were thus consistent with standard auroral activity, whereas S_3 indicated a more unusual case, possibly driven by internal dynamics. The detailed wave properties and characteristics of the three identified sources are listed in Table 1. Hereafter, we focus on events S_3 and S_1 as illustrative examples. A polar projection of the magnetic footprint of these sources is provided in fig. S3, which shows that they are additionally colocated with the average northern ultraviolet (UV) aurorae, as observed by the Hubble Space Telescope (HST) throughout 2017 (29). Event S_3 displayed the most intense radio emission and benefited from

Table 1. Properties of the three R-X mode SKR low-frequency sources identified during the Cassini ring-grazing orbits. Where provided, uncertainties are one standard deviation.

SKR source	S_1	S_2	S_3
Time range (UT)	2016-339	2016-346	2017-066
	08:42:50–08:59:54	13:33:26–13:34:30	15:11:48–15:17:25
	(orbit 251)	(orbit 252)	(orbit 264)
Cassini ephemeris:			
Latitude (°)	+61.9–60.9	+59.6–59.5	+54.0–53.1
LT (hours)	9.06–9.41	9.72–9.74	10.32–10.43
Distance to Saturn's center (R_S)	4.47–4.31	4.15–4.14	3.63–3.58
Altitude along the flux tube (R_S)	3.65–3.49	3.33–3.32	2.84–2.79
from the 1-bar atmospheric level			
f_{ce} (kHz)	13–14	15	22–23
Δf (kHz)	0.1–0.4	<1.5	<2
Size range (km)	240–3400	1300	6050
	(9 subsources)	(1 source)	(1 source)
Mean f_{SKR}/f_{ce} ratio	0.976 ± 0.006	0.975 ± 0.008	0.989 ± 0.004
(range)	(0.965–0.998)	(0.968–0.987)	(0.978–0.995)
Mean electron energy (keV)	11 ± 3	12 ± 4	6 ± 3
(range)	(1–17)	(7–16)	(3–11)
Median Poynting flux (W/m²)	5.9 10⁻¹³	1.2 10⁻¹³	7.3 10⁻¹²
(range)	(2.6 10⁻¹⁴–2.7 10⁻¹¹)	(9.1 10⁻¹⁴–1.6 10⁻¹²)	(2.0 10⁻¹³–2.3 10⁻⁸)
Median electric field amplitude (mV/m)	0.033 ± 0.032	0.014 ± 0.011	0.292 ± 0.884
(range)	(0.004–0.142)	(0.008–0.035)	(0.012–4.211)
Beaming angle (°)	93 ± 9	86 ± 16	91 ± 16
θ = (**k**,**B**)			
Upward current density (nA/m²)	157	171	105

coordinated HST observations, whereas event S_1 was sampled by RPWS-WBR (wideband receiver) waveform measurements.

Example SKR source crossings

Radio, plasma, and magnetic field measurements during events S_3 and S_1 are shown in Figs. 1 and 2, respectively (S_2 is shown in fig. S2). SKR is the patchy bright emission observed above 10 kHz in Figs. 1A and 2A and fig. S2A (dynamic spectrum of the wave Poynting flux S), with dominant right-handed (RH) circular polarization in Figs. 1B and 2B and fig. S2B (dynamic spectrum of the normalized degree of circular polarization V) indicative of northern R-X mode. Some weaker left-handed (LH) polarized SKR, indicative of left-hand ordinary (L-O) mode, was additionally observed at the low-frequency edge of the R-X mode SKR toward the end of the intervals plotted in Figs. 1 and 2 and fig. S2, preceding the periapsis. The weakly polarized emission visible below 10 kHz after 15:30 UT (Universal Time) on Fig. 1, A and B, is identified as auroral hiss, a whistler-mode emission. Narrow-banded long-duration and drifting short-duration emissions observed below 35 kHz are not investigated in our analysis. Localized SKR R-X mode LF emission is tangent to the f_{ce} curve near the middle of each interval. Condition $f_{SKR} < f_{ce}$ (Figs. 1C and 2C and fig. S2C) is then used to define the overall extent of the source region. During event

S_3 (Fig. 1, A to C), a single SKR source was continuously observed from 15:11:48 to 15:17:25 UT, corresponding to a 6050-km distance along the spacecraft trajectory. During event S_1 (Fig. 2, A to C), multiple SKR sources were observed between 08:42:50 and 08:59:54 UT.

Figure 3 shows restricted portions of Fig. 2A at higher time-frequency resolution obtained from RPWS-WBR waveform measurements (2). Faint, localized, remote SKR emissions observed well above f_{ce} (Fig. 3A) display recurrent drifting substructures with scarce positive and prominent negative rates of ~1 kHz/min, consistent with previous SKR waveform observations (30). An enlargement of the 08:00-09:10 UT interval (Fig. 3B) reveals the time-frequency structure of the radio source. Whereas Fig. 1A suggested a single emission pattern with a bandwidth of a few kHz lasting for nearly 2 hours, Fig. 3B shows that it splits into several subcomponents of variable durations (down to a few min) and bandwidths. Those with frequencies slightly, but clearly, above f_{ce} likely correspond to sources on nearby flux tubes, while only the component strictly tangent to and below the f_{ce} curve unambiguously indicates a local source. The overplotted f_{SKR} profile (as determined in Fig. 2C) provides, despite its lower temporal resolution, a one-to-one correspondence between the brief episodes of $f_{SKR} <$ f_{ce} and the observed SKR bursts (including the central event between 08:45 and 08:50 UT and

the shorter bursts beside it). This agreement validates the method employed to determine f_{SKR}. For this specific event, we therefore considered nonconsecutive RPWS-HFR episodes with $f_{SKR} < f_{ce}$ as isolated subsources as well. The overall source region of event S_1 thus decomposes into nine SKR subsources. Their horizontal size along the spacecraft trajectory, and across the encountered flux tubes, ranged from 240 to 3400 km. Their ~100- to 400-Hz bandwidth Δf characterizes very narrow-banded emissions with $\Delta f / f_{ce}$ 0.008 to 0.03, and thus corresponds to radiating structures that extended vertically 700 to 2800 km along the magnetic flux tubes.

Perpendicular emission and energy of source electrons

Figures 1 and 2C and fig. S2C (right) show the kinetic energy of CMI-unstable electrons derived from the measurements of $f_{SKR} < f_{ce}$, assuming perpendicular emission at the source and thus $f_{SKR} = f_{ce}\sqrt{1 - v^2/c^2}$, as for the southern event of 2008-291. To check this assumption, we analyzed the wave parameters derived from the goniopolarimetric (direction-finding) analysis of RPWS-HFR three-antenna measurements (2). These consist of the wave Stokes parameters S, Q, U, and V (31) and the $\boldsymbol{k}$-vector direction. From the latter, we also retrieved the 3D locus of the radio source, from the intersection of the $\boldsymbol{k}$ line-of-sight with a model iso-$f = f_{ce}$ surface (assuming straight-line propagation, which is reasonable at high latitude), and its beaming angle $\theta = (\boldsymbol{k}, \boldsymbol{B})$, where $\boldsymbol{B}$ is the magnetic field vector at the source (4, 8, 12, 32).

Figure 4 displays the variation of the beaming angle $\theta(f)$ of events S_3 and S_1 for the time intervals of Figs. 1 and 2 using a standard data selec-

tion (2) for RH (LH) polarized waves, and thus R-X (L-O) mode. In agreement with previous studies of the SKR beaming angle (8, 23, 32, 33), $\theta(f)$ of R-X mode emission smoothly rises from 60 ± 25° at 800 kHz to 85°±15° at 30 kHz, where the uncertainty on θ is dominated by the scatter of data points. Figure S4E shows an alternative representation of $\theta(f)$ in the time-frequency plane. This systematic change from perpendicular to oblique emission with increasing frequency is most likely due to refraction of R-X mode waves on the nearby iso-f_X surface, where $f_X \sim f_{ce}$ is the R-X mode cutoff frequency (8), as proposed for auroral radio emissions of Earth and Jupiter (34, 35). In this case, the apparent R-X mode beaming angle should vary as a function of the $\boldsymbol{k}$-vector direction projected in a plane perpendicular to $\boldsymbol{B}$, with the strongest refraction expected for wave propagation toward the

Fig. 1. Cassini radio, plasma, and magnetic measurements acquired on day 2017-066 between 13:00 and 17:00 UT (event S_3) in the northern dawn-side sector. (A and B) Dynamic spectra of wave Poynting flux S and normalized degree of circular polarization V, respectively, derived from two- and three-antenna RPWS-HFR 16-s measurements over 3.5 to 1500 kHz (2). $V = -1$ (+1) refer to RH (LH) polarization, and thus to R-X (L-O) mode emission from the northern hemisphere. The white dashed lines indicate the electron cyclotron frequency f_{ce} as derived from MAG data. R-X mode SKR around 20 kHz comes close to f_{ce} after 15:00 UT. (C) Ratio of the SKR low-frequency cutoff f_{SKR} to f_{ce} (2). Values $f_{SKR}/f_{ce} < 1$ define one SKR source crossing between 15:11 and 15:18 (orange-shaded region on (C) and (D), extended by vertical dotted-dashed lines in the other panels). The right-handed gray scale provides the kinetic electron energy inferred from $f_{SKR} = f_{ce}\sqrt{1-v^2/c^2}$, assuming perpendicular emission. (D) Characteristic frequencies comparing f_{SKR} (solid black line), f_{ce}, and $f_{ce}/10$ (dashed black lines) and the electron plasma frequency f_{pe} as directly derived from RPWS Langmuir probe 32-s measurements (gray profile) together with a lower limit $f_{pe\ min}$ estimated from the auroral hiss upper frequency cutoff measured with RPWS-MFR 64-s measurements (2) (red profile). (E) Magnetic azimuthal component $B\varphi$, as from 1-min averaged MAG measurements in spherical coordinates. The green-shaded area marks a region of positive slope, indicative of an upward-directed current region. The SKR source region starts at the beginning of the upward current region and ends before Cassini exits it, when f_{pe} suddenly rises above $f_{ce}/10$.
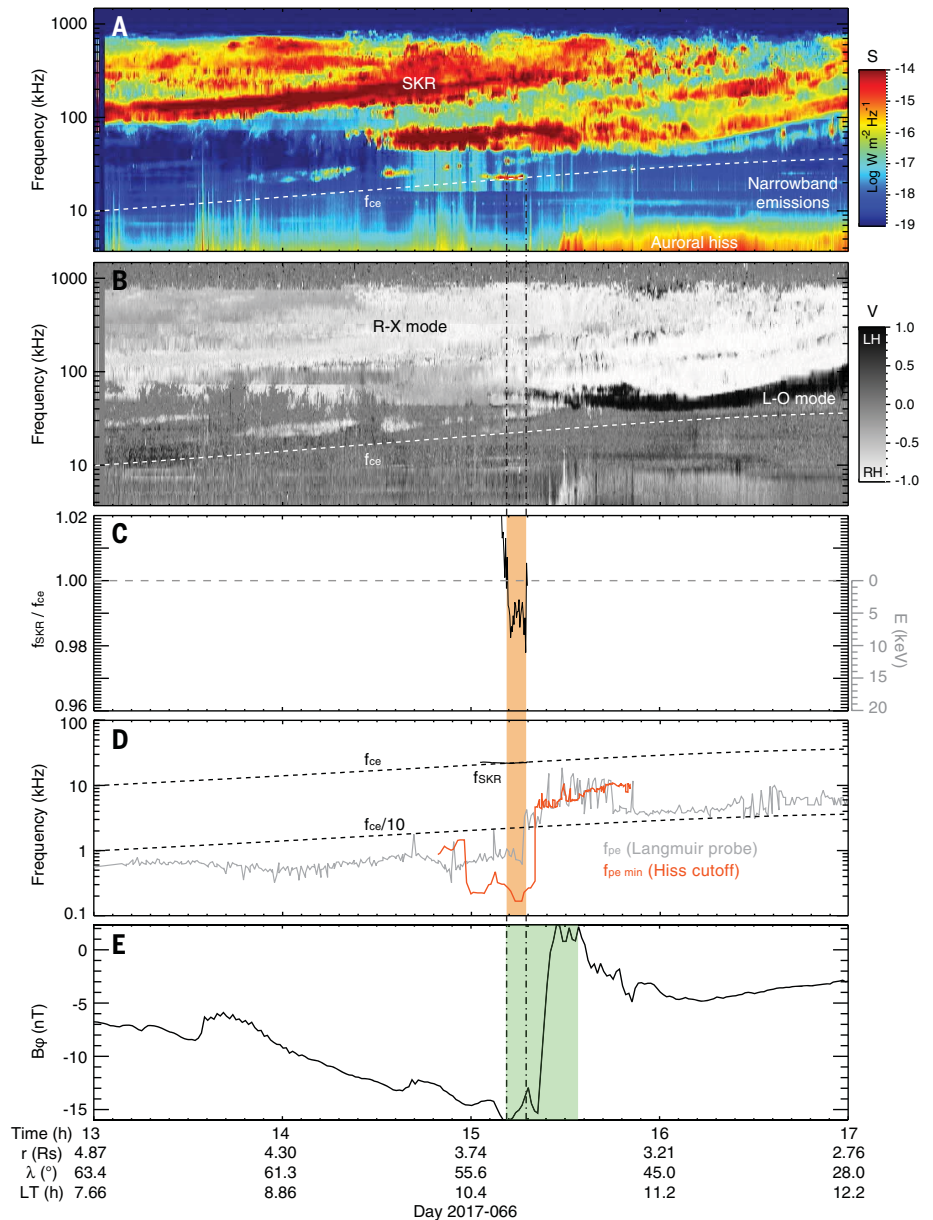
equator. L-O mode SKR was also observed, over an extended spectral range of 30 to 100 kHz, with $\theta(f)$ remaining confined above 75° and with a lower scattering than the R-X mode. The L-O mode cutoff frequency f_O is f_{pe}, which was in this case much lower than f_{ce} (Figs. 1 and 2D), so no similar refraction on the iso-f_O surface is expected. This interpretation implies that $\theta(f)$ measures the apparent (real) beaming angle of SKR R-X (L-O) mode affected (unaffected) by refraction close to the source. Although they differ at high frequencies, both remote observations of R-X and L-O mode $\theta(f)$ indicate quasi-perpendicular emission at 30 kHz, toward frequencies where the local radio sources have been sampled.

A second method provides a direct measurement of the wave emission angle within the source from its polarization state. For perpendicular cyclotron emission, the polarization ellipse axial ratio $AR = (T - L)/V$, where $T = \sqrt{Q^2 + U^2 + V^2}$ and $L = \sqrt{Q^2 + U^2}$ are the total and linear polarization degrees (*31*), can be approximated to first order as $\cos \theta$ (*36*). Figures 1 and 2B and fig. S4, A to D, show that the emission is strongly linearly polarized at the source, as observed during the southern event of 2008-291. Measurement of the mean AR in each SKR source of the three events S_1, S_2, and S_3, restricting to the two HFR frequencies encompassing f_{ce} with standard data selection (identical to that used in Fig. 5C, discussed below), gives $AR = -0.02 \pm 0.26$, 0.06 ± 0.28, and -0.05 ± 0.15, which results in $\theta = 91 \pm 16°$, $86 \pm 17°$, and $93 \pm 9°$, respectively, all consistent with perpendicular emission.

The measured values of f_{SKR} can therefore be safely inverted to derive kinetic energies of CMI-unstable electrons (Figs. 1C and 2C, fig. S2C, and Table 1). On average, f_{SKR} reached a level of −2% from f_{ce} with a minimum value of −3.5%. The corresponding electron energies spanned the 1- to 17-keV range, with mean values between 6 and 12 keV depending on the event and a standard deviation of 3 to 4 keV, larger than the 2-keV uncertainty arising from the f_{SKR} measurements. No correlation is found between the obtained electron energies and the observed wave intensities, measured between a few 0.01 and a few mV m^{-1}.

Auroral plasma conditions

We now investigate the auroral plasma conditions to assess the validity of CMI condition (ii). Figures 1D and 2D compare the characteristic frequencies f_{SKR}, f_{ce}, and f_{pe}. f_{pe} was derived from Langmuir probe (LP) 32-s measurements and compared to the upper frequency cutoff of auroral hiss derived independently from the RPWS-MFR (medium frequency receiver) 64-s measurements. The LP measures the total electrical current carried by the ambient plasma from voltage sweeps, from which the local electron density N and thus f_{pe} are derived (*2*). The voltage sweep resolution leads to a typical uncertainty on f_{pe} of less than a factor of 2. Auroral hiss is radiated upward from below the spacecraft and propagating beneath f_{pe}, so that its upper fre-
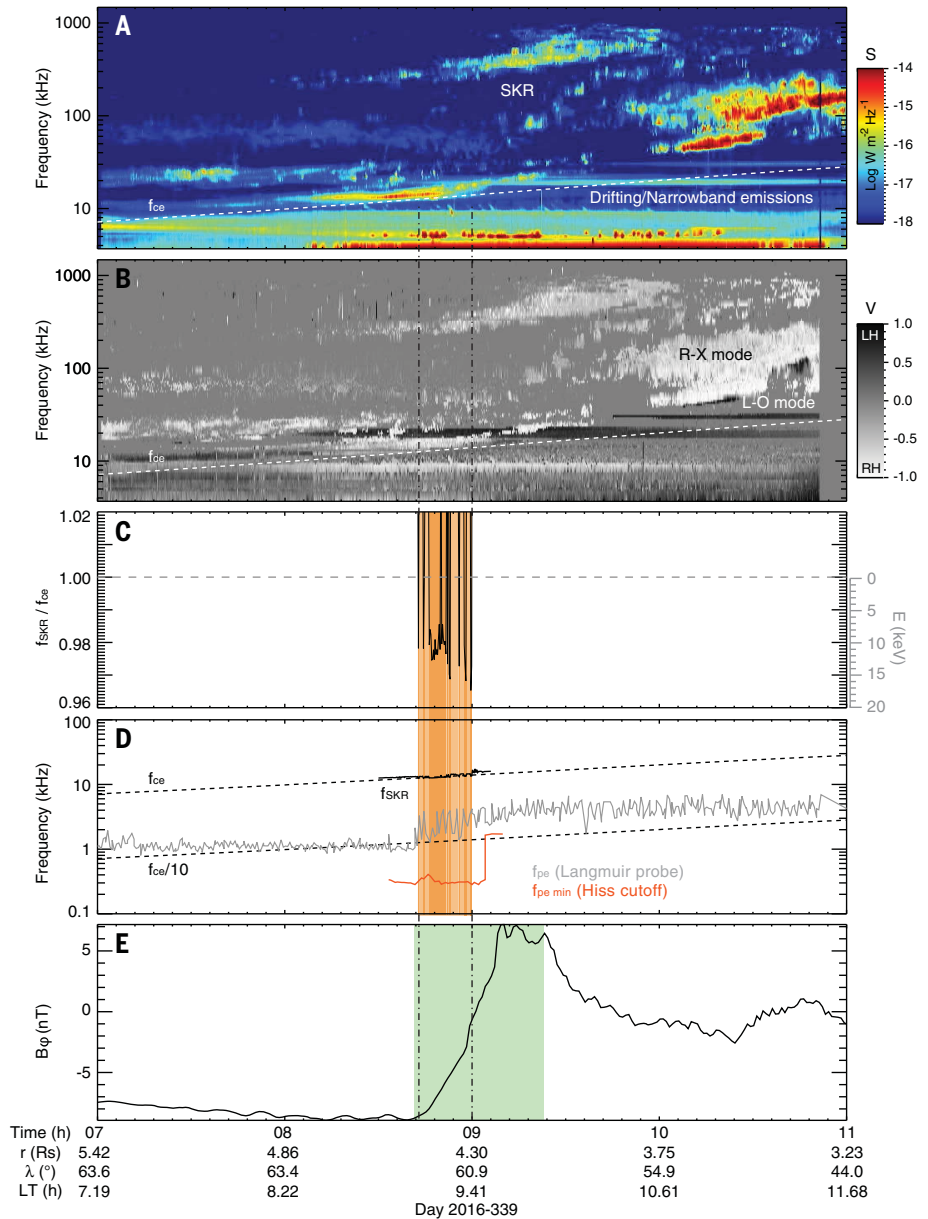
quency cutoff, when marking a sharp transition, is a proxy of f_{pe} when $f_{pe} < f_{ce}$. The observed hiss emissions were generally damped and exhibited a smoothed cutoff, so we interpret the fitted frequencies as a lower limit on f_{pe}, labeled $f_{pe\,min}$. In Figs. 1D and 2D, the $f_{pe\,min}$ profiles were close to, and generally below, the LP-derived f_{pe} profiles. For event S_1 (Fig. 1D), f_{pe}/f_{ce} was about 0.03 across the whole source region, which ended when the value of f_{pe} suddenly rose by a factor of 4 at 15:18 UT (and $f_{pe\,min}$ by a factor of 13 at 15:20 UT), exceeding the $f_{ce}/10$ threshold for CMI condition (ii). For event S_3 (Fig. 2D), a similar density gradient was observed in both data-

sets. The hiss cutoff frequency $f_{pe\,min}$ rose by a factor of 5 at 09:04 UT, again shortly after exiting the SKR source region at 09:00 UT. The LP-derived f_{pe}, determined at a higher time resolution, reveals more complex variability: Although f_{pe} rose by a factor of 4 at 08:42, it then showed large-scale fluctuations of a factor of ~3 (~2) up to (after) 09:00 UT. The SKR subsources (sampled at a better cadence) match the local minima of f_{pe}, suggesting that small-sized radio sources were colocated with local density cavities. Similar results were observed during event S_2 (fig S2D), despite lower time-resolution measurements of f_{pe}.

Fig. 2. As for Fig. 1, but for measurements acquired on day 2016-339 between 07:00 and 11:00 UT (event S_1) in the northern dawn-side sector. (**A** to **E**) Nine SKR sources near 13 kHz were encountered successively between 08:43 and 09:00. The overall interval is delimited by a light orange-shaded region, while the individual SKR sources are indicated by dark orange-shaded areas.
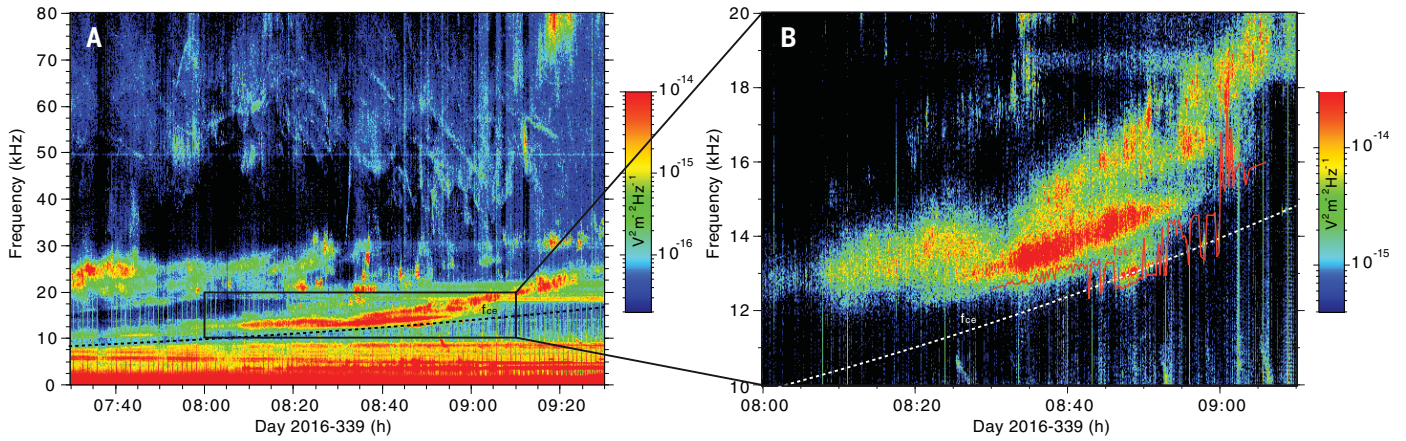
Fig. 3. High-resolution dynamic spectra of event S_1 reconstructed from Cassini radio electric waveform measurements taken on 2016-339. The spectra were acquired with the RPWS-WBR receiver over the 0- to 80-kHz range (2). (**A**) Reconstructed dynamic spectrum between 07:30 and 09:30 UT. The dashed line indicates f_{ce}. (**B**) Enlargement of the encountered local SKR source. The solid red line indicates f_{SKR}, as derived from RPWS-HFR measurements in Fig. 2D. It is in agreement with high-resolution WBR measurements of SKR emission close to and below f_{ce}.
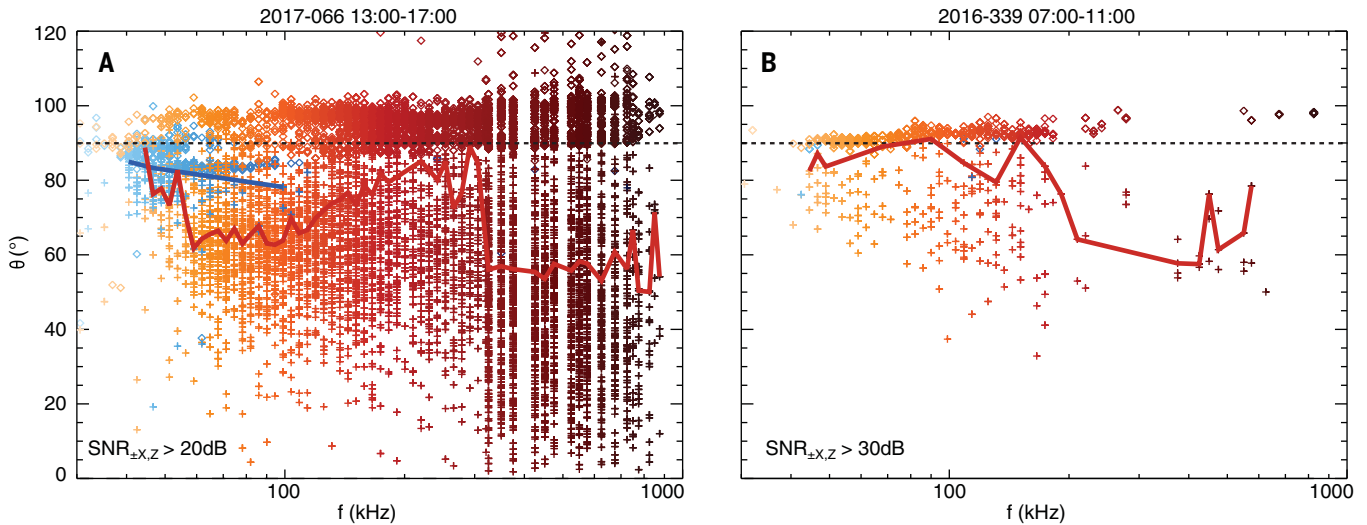
Fig. 4. SKR beaming angle at the source as a function of frequency. (**A**) Time interval from 13:00 to 17:00 UT on 2017-066 (event S_3) encompassing the SKR source crossed around 15:15 UT. The beaming angle is defined as $\theta = (\boldsymbol{k}, \boldsymbol{B})$, where $\boldsymbol{k}$ is the wave vector determined remotely from RPWS-HFR three-antenna measurements, and $\boldsymbol{B}$ the magnetic field vector at the source (2). A standard data selection was applied with $T > 0.85$, $|z_r| < 0.05$, and signal-to-noise ratio $SNR_{\pm X,Z} > 20$ dB. The color scale refers to the wave frequency, with red (blue) symbols corresponding to RH (LH) polarized waves and thus to R-X (L-O) mode. Crosses (diamonds) indicate $\boldsymbol{k}$ directions that intercept (do not intercept) their iso-$f = f_{ce}$ surface, assuming straight-line propagation. Red and blue lines indicate the median value of θ, derived at each frequency for which the number of crosses exceeds the number of diamonds (7). The dotted line marks emission perpendicular to the local magnetic field vector. (**B**) Time interval from 07:00 to 11:00 UT on 2016-339 (event S_1) encompassing the multiple SKR sources crossed around 08:50 UT. The data selection was identical to that of (A) except that $SNR_{\pm X,Z} > 30$ dB to better remove faint non-SKR narrow-banded emissions observed up to 40 kHz (2). Both panels show that θ increases from $60 \pm 25°$ at 800 kHz to $85 \pm 15°$ at 30 kHz, consistent with quasi-perpendicular emission at the source.

Figures 1E and 2E and fig. S2E show the azimuthal component of the magnetic field measured from 1-min averaged MAG data. They indicate upward currents in intervals dominated by a positive slope. Each SKR source region started at (but ended before) the beginning (end) of the upward current region. The upward current density was estimated to be 106, 171, and 157 nA m^{-2} for events S_1, S_2, and S_3, respectively, well above the average of 80 nA m^{-2} derived from all the ring-grazing northern upward current regions (37).

Additional information on the correspondence between auroral emissions and upward currents is apparent in Fig. 5, which maps the spatial distribution of SKR sources during event S_3, along with the northern UV aurorae simultaneously observed by HST (29) on 2017-066 (17 March) over 15:27-16:21 UT (corrected for the light travel time). Figure 5A displays the distribution of SKR emissions observed over the same time interval as in Fig. 1, as seen from Cassini. As expected for cyclotron emission, SKR

lower- (higher-) frequency sources are observed at larger (closer) distances from the planet. Figure 5B displays in a polar view the magnetic footprint of radio sources visible in Fig. 5A. The R-X mode footprints map a circumpolar auroral oval visible from 04:00 to 22:00 LT. Its latitudinal width of about 8° to 10° is dominated by the scattering of goniopolarimetric results. This longitudinally extended range derives from the LT range swept by the spacecraft during the investigated interval. Movie 1 displays an animation

Fig. 5. Spatial distribution of SKR sources and UV aurorae. (**A**) 2D locus of SKR sources in the sky plane as seen from Cassini, from RPWS-HFR three-antenna measurements of **k** directions (2) on 2017-066 13:00–17:00 UT (event S_3). The applied data selection was identical to that used in Fig. 4A, except that $SNR_{\pm X,Z} > 40$ dB for clarity. The color scale and definition of symbols are identical to those of Fig. 4A. The red planetary meridian indicates noon. The typical 2° uncertainty on **k** measurements is displayed by the bottom-right ellipse. (**B**) Polar view of the magnetic footprint of radio sources displayed in (A) as a function of planetocentric latitude and LT. Error bars are not represented for clarity but are similar to those studied in (12, 32). The dotted-dashed curved lines display radio horizons at extremal frequencies, beyond which a radio source cannot be observed. The double green arrow indicates the Cassini LT range swept during the interval. The gray line plots the associated Cassini magnetic footprint, whose orange and green portions indicate the crossing of SKR source and of the upward current region identified in Fig. 1. (**C**) Same as (B) but for the SKR source observed from 09:00 to 09:20 UT between 20 and 27 kHz. The data selection was slightly relaxed with $T > 0.85$, $|z_r| < 0.2$ and $SNR_{\pm X,Z} > 20$ dB to maximize statistics. Cassini's LT is indicated by a green dotted-dashed arrow. The radio source footprints coincide with the crossed SKR source (orange portion of the gray line). (**D**) Polar view of Saturn's H_2 aurorae observed with the Hubble Space Telescope on day 2017-066 from 15:27 to 16:21 UT, after

Cassini FOV (120°)

Magnetic polar projections

correcting for light travel time. The background-subtracted image was projected onto the 1100-km-altitude surface as a function of planetocentric coordinates and expressed in kilo-rayleighs (kR) of H_2 (2). The gray line and its colored portions are identical to those of (B) and (C). The upward current layer (green) matches the main auroral oval, while the SKR source crossed (orange) only matches the poleward portion of it.
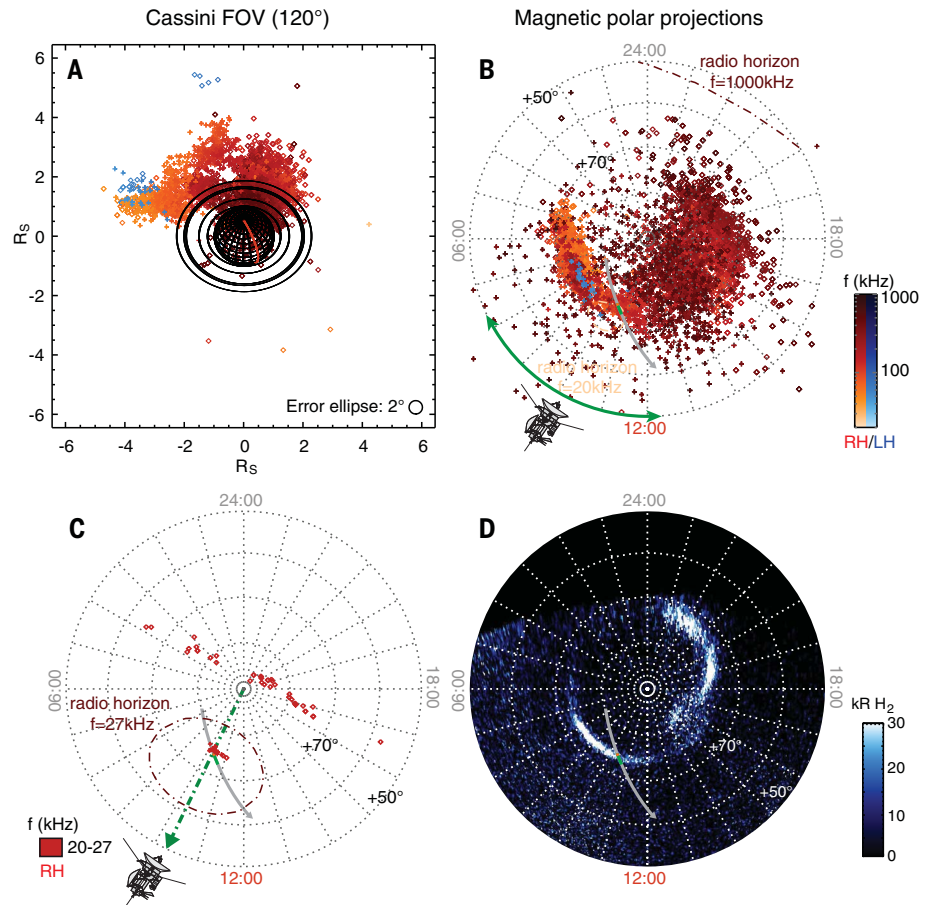
of Fig. 5, A and B, and illustrates how the spatial distribution of detected sources varies with the time-variable position of the spacecraft. The L-O mode footprints are well clustered and precisely colocated with the R-X mode footprints between 08:00 and 10:00 LT. The comparison with Fig. 5D illustrates that SKR sources are colocated with the UV auroral oval (see fig. S5 for a superimposition of both panels). This correspondence is visible both on the dawn-side sector, where the UV oval is thin and well defined between 06:00 and 12:00 LT from +72° to +75° latitudes, and on the dusk-side sector, where the UV aurorae are more spread in latitude between 14:00 and 23:00 LT and include a poleward arc beyond +80° between 14:00 and 18:00 LT. The Cassini footprint trajectory is displayed by the gray arrow in Fig. 5, B to D, over the 13:00–17:00 UT interval. Its colored portions indicate the upward current region and the SKR source region identified in Fig. 1. The upward current layer matches the main UV auroral oval in size, while the SKR source was traversed along a smaller, poleward, portion of it. This can be better seen in Fig. 5C, which is similar to Fig. 5B except that it only plots local radio sources,
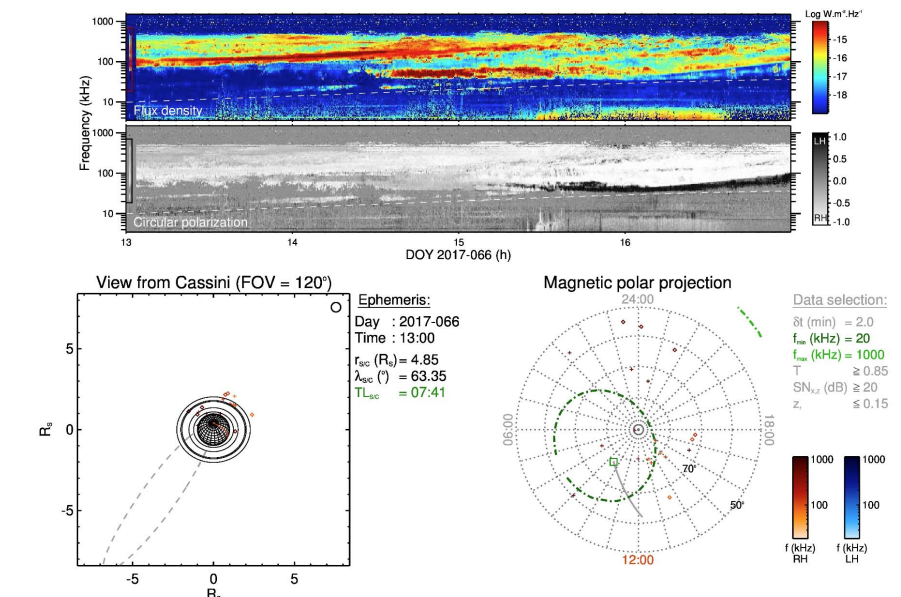
Movie 1. Animated view of the spatial distribution of SKR sources in a format identical to that of Fig. 5, A and B. The only differences are the exposure time, here fixed to 2 min for each frame, and the data selection criteria, here slightly relaxed with respect to Fig. 5, A and B, to maximize statistics (2).
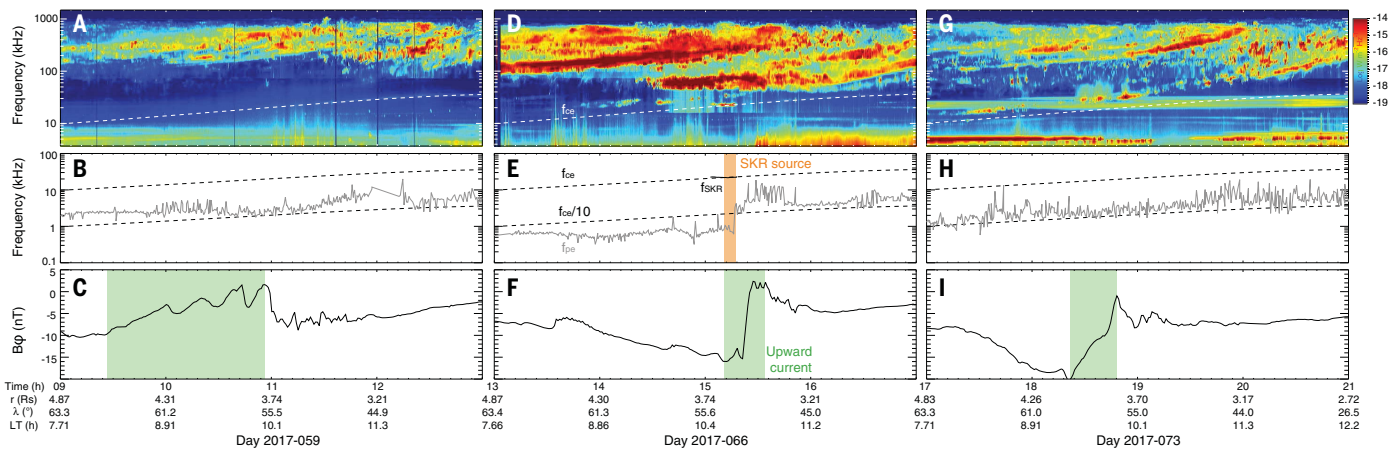
Fig. 6. Cassini radio, plasma, and magnetic measurements acquired during three successive auroral passes with similar trajectories. (**D** to **F**) Identical to Fig. 1, A, D, and E, covering the interval 2017-066 from 13:00 to 17:00 UT encompassing a SKR source crossing (orange-shaded region). (**A** to **C**) and (**G** to **I**) Same as (D) to (F) but for the intervals 2017-059 09:00-13:00 UT and 2017-073 17:00-21:00 UT (i.e., the orbit before and after), respectively. No SKR source was detected during these intervals, for which f_{pe} was always larger than $f_{ce}/10$.

radiated near f_{ce} (2). Again, the footprints of R-X mode located sources map to the Cassini trajectory and only to the inward portion of the main oval and associated upward current layer.

Implications for the generation of Saturn's auroral radio emissions

We now discuss the average properties of SKR LF emissions as a whole, in the CMI frame. The identification of only three SKR sources in the dawn-side sector and none in the dusk-side sector brings a direct in situ confirmation to the LT dependence of SKR spectrum (here studied during quiet solar wind conditions), with lowest frequencies at dawn (16, 24). The small number of radio sources identified along orbits with very similar trajectories and their limited extent additionally indicate time-variable generation conditions.

In all three cases, the sampled R-X mode emission was found to be amplified nearly perpendicularly to the local magnetic field, with emission frequency clearly below f_{ce} supplied by CMI-unstable electrons of 6- to 12-keV mean energies. Direct perpendicular emission through CMI requires specific shell-type distribution functions of the accelerated electrons in the velocity plane, such as those already measured for the two southern SKR sources crossed in 2008 (9, 13). The situation at Saturn thus directly compares to the terrestrial case, where AKR sources are commonly found to be associated with trapped, shell- or horseshoe-type distributions (3, 38, 39). It differs from the situation at Jupiter, which just started to be investigated in situ by the Juno spacecraft, where the hectometer and decameter radio emissions instead appear to be produced at oblique angles from the local magnetic field by loss cone electron distribution functions (40, 41). The presence of 6- to 12-keV electron beams with such distribution functions at 3.5 to 4.5 R_S distances from Saturn's center, or equivalently 2.8 to 3.7 R_S above the atmosphere along flux tubes (Table 1), implies that

at least part of the acceleration by upward currents occurred farther along the field lines, which constrains models of current-voltage relationships (42).

The general agreement with the CMI mechanism relies on fulfilling both CMI conditions. The three SKR sources encountered by Cassini matched upward currents with current densities larger than the average (37), consistent with an acceleration region extending to higher altitudes and thus satisfying CMI condition (i). Then, while the spacecraft entered the northern SKR source region when it encountered an upward current region, it exited it when f_{pe} suddenly rose, exceeding the typical $f_{ce}/10$ threshold. After exiting the source, the spacecraft remained for some time inside the upward current region, which matches the main UV oval across the Cassini trajectory. This suggests that at 3.5 to 4.5 R_S distances, SKR emission is primarily controlled by the electron plasma density N through CMI condition (ii), which quenches the radiation when f_{pe}/f_{ce} typically exceeds 0.1. According to the Knight relationship (43) and assuming a constant current density, larger N is also expected to decrease electron acceleration and weaken CMI condition (i).

Figure 6 shows radio, plasma, and magnetic measurements for three successive, quasi-identical, passes of the spacecraft into the northern dawn-side auroral region. Figure 6, D to F, correspond to event S_3 (orbit 264), while Fig. 6, A to C and G to I, correspond to the previous (orbit 263) and the following (orbit 265) auroral passes. The spacecraft did not fly across any local SKR source during orbits 263 and 265, while it encountered regions of upward current in both cases with current densities of 29 and 108 nA m^{-2}. On orbit 265, the SKR intensity was relatively high and its spectrum reached frequencies as low as 20 kHz, while the upward current density was as strong as that of orbit 264. Instead, on orbit 263, SKR was comparatively faint, with a spectrum confined to higher frequencies and a lower upward

current density. This suggests that CMI condition (i), which requires unstable electrons at 3.6 R_S, was at least satisfied for orbit 265. For both intervals, however, f_{pe} was systematically larger than $f_{ce}/10$ within the upward current region, in contrast with orbit 264 (event S_3), indicating that the mean level of N over hours-long intervals strongly varies with time from pass to pass. These results thus indicate that CMI condition (ii) was not fulfilled for orbits 263 and 265 and likely quenched SKR LF emission during orbit 265.

The origin of time-variable magnetospheric plasma densities at the altitude of LF SKR sources has now to be elucidated. The asymmetrical plasmapause-like boundary, a transition from high to low plasma densities with increasing latitudes that rotates at the northern SKR period, is a plausible source for time-variable N (44). On a shorter time scale, Fig. 1 does not display any Earth-like plasma cavity, as already noticed for the 2008-291 southern event (4). However, Fig. 2 (and possibly fig. S2) shows small-sized, recurrent, drops of f_{pe} colocated with SKR sources for event S_1 (and S_2). This suggests that acceleration features could coincide with localized radio sources, as at Earth. Definite conclusions, however, rely on knowing whether the plasma region was dominated by hot electrons (such as on day 2008-291) or could have included a cold plasma component sensitive to local potential drops and able to map plasma cavities. As the CAPS experiment was not operating during these orbits, these issues remain unresolved.

Finally, the very narrow-banded nature of SKR sources, particularly obvious during event S_1 (Fig. 3B), is consistent with either a nonsaturated linear wave growth, as predicted by the CMI theory and measured in laboratory [e.g., (45)], or with saturation by coherent nonlinear trapping, previously assumed in models of the SKR spectrum (46). However, the emission levels may be too low to reach saturation, and the observed wave intensities (Table 1) are also consistent with linear growth.

REFERENCES AND NOTES

1. L. Lamy, The Saturnian Kilometric Radiation before the Cassini Grand Finale, in *Planetary Radio Emissions VIII*, G. Fischer, G. Mann, M. Panchenko, P. Zarka, Eds. (Austrian Academy of Sciences Press, Vienna, 2017), pp. 171–190.
2. Materials and methods are available as supplementary materials.
3. R. A. Treumann, The electron-cyclotron maser for astrophysical applications. *Astron. Astrophys. Rev.* **13**, 229–315 (2006). doi: 10.1007/s00159-006-0001-y
4. L. Lamy et al., Properties of Saturn kilometric radiation measured within its source region. *Geophys. Res. Lett.* **37**, L12104 (2010). doi: 10.1029/2010GL043415
5. E. J. Bunce et al., Extraordinary field-aligned current signatures in Saturn's high-latitude magnetosphere: Analysis of Cassini data during revolution 89. *J. Geophys. Res.* **115**, A10238 (2010). doi: 10.1029/2010JA015612
6. W. S. Kurth et al., A close encounter with a Saturn kilometric radiation source region, in *Planetary Radio Emissions VII*, H. O. Rucker, W. S. Kurth, P. Louarn, G. Fischer, Eds. (Austrian Academy of Sciences Press, Vienna, 2011), pp. 75–85.
7. P. Schippers et al., Auroral electron distributions within and close to the Saturn kilometric radiation source region. *J. Geophys. Res.* **166**, A05203 (2011). doi: 10.1029/2011JA016461
8. L. Lamy et al., Emission and propagation of Saturn kilometric radiation: Magnetoionic modes, beaming pattern, and polarization state. *J. Geophys. Res.* **116**, A04212 (2011). doi: 10.1029/2010JA016195
9. R. L. Mutel et al., CMI growth rates for Saturnian kilometric radiation. *Geophys. Res. Lett.* **37**, L19105 (2010). doi: 10.1029/2010GL044940
10. A. Hilgers, The auroral radiating plasma cavities. *Geophys. Res. Lett.* **19**, 237–240 (1992). doi: 10.1029/91GL02938
11. J. D. Menietti et al., Saturn kilometric radiation near a source center on day 73. In *Planetary Radio Emissions VII*, H.O. Rucker, W. S. Kurth, P. Louarn, G. Fischer, Eds. (Austrian Academy of Sciences Press, Vienna, 2011), pp. 87–95.
12. L. Lamy et al., An auroral oval at the footprint of Saturn's kilometric radio sources, colocated with the UV aurorae. *J. Geophys. Res.* **114**, A10212 (2009). doi: 10.1029/2009JA014401
13. J. D. Menietti et al., Analysis of Saturn kilometric radiation near a source center. *J. Geophys. Res.* **116**, A12222 (2011). doi: 10.1029/2011JA017056
14. W. S. Kurth et al., An Earth-like correspondence between Saturn's auroral features and radio emission. *Nature* **433**, 722–725 (2005). doi: 10.1038/nature03334; pmid: 15716947
15. W. S. Kurth et al., Saturn kilometric radiation intensities during the Saturn auroral campaign of 2013. *Icarus* **263**, 2–9 (2016). doi: 10.1016/j.icarus.2015.01.003
16. L. Lamy et al., Saturn kilometric radiation: Average and statistical properties. *J. Geophys. Res.* **113** (A7), A07201 (2008). doi: 10.1029/2007JA012900
17. S. V. Badman, S. W. H. Cowley, L. Lamy, B. Cecconi, P. Zarka, Relationship between solar wind corotating interaction regions and the phasing and intensity of Saturn kilometric radiation bursts. *Ann. Geophys.* **26**, 3641–3651 (2008). doi: 10.5194/angeo-26-3641-2008
18. D. A. Gurnett et al., Discovery of a north-south asymmetry in Saturn's radio rotation period. *Geophys. Res. Lett.* **36**, L16102 (2009). doi: 10.1029/2009GL039621
19. D. G. Mitchell et al., Recurrent energization of plasma in the midnight-to-dawn quadrant of Saturn's magnetosphere, and its relationship to auroral UV and radio emissions.

Planet. Space Sci. **57**, 1732–1742 (2009). doi: 10.1016/j.pss.2009.04.002
20. C. M. Jackman et al., On the character and distribution of lower-frequency radio emissions at Saturn and their relationship to substorm-like events. *J. Geophys. Res.* **114**, A08211 (2009). doi: 10.1029/2008JA013997
21. C. M. Jackman et al., In situ observations of the effect of a solar wind compression on Saturn's magnetotail. *J. Geophys. Res.* **115**, A10240 (2010). doi: 10.1029/2010JA015312
22. L. Lamy, Variability of southern and northern SKR periodicities, in *Planetary Radio Emissions VII*, H.O. Rucker, W.S. Kurth, P. Louarn, G. Fischer, Eds. (Austrian Academy of Sciences Press, Vienna, 2011), pp. 39–50.
23. L. Lamy et al., Multispectral simultaneous diagnosis of Saturn's aurorae throughout a planetary rotation. *J. Geophys. Res.* **118**, 4817–4843 (2013). doi: 10.1002/jgra.50404
24. T. Kimura et al., Long-term modulations of Saturns auroral radio emissions by the solar wind and seasonal variations controlled by the solar ultraviolet flux. *J. Geophys. Res.* **118**, 7019–7035 (2013). doi: 10.1002/2013JA018833
25. J. J. Reed, C. M. Jackman, L. Lamy, W. S. Kurth, D. K. Whiter, Low Frequency Extensions of the Saturn Kilometric Radiation as a proxy for magnetospheric dynamics. *J. Geophys. Res.* **123**, 443–463 (2018). doi: 10.1002/2017JA024499
26. D. A. Gurnett et al., The Cassini Radio and Plasma Wave Investigation. *Space Sci. Rev.* **114**, 395–463 (2004). doi: 10.1007/s11214-004-1434-0
27. M. K. Dougherty et al., The Cassini magnetic field investigation. *Space Sci. Rev.* **114**, 331–383 (2004). doi: 10.1007/s11214-004-1432-2
28. D. T. Young et al., Cassini Plasma Spectrometer investigation. *Space Sci. Rev.* **114**, 1–112 (2004). doi: 10.1007/s11214-004-1406-4
29. L. Lamy et al., Saturn's northern aurorae at solstice from HST observations coordinated with Cassini's Grand Finale. *Geophys. Res. Lett.* **45**, (2018). doi: 10.1029/2018GL078211
30. W. S. Kurth et al., High spectral and temporal resolution observations of Saturn kilometric radiation. *Geophys. Res. Lett.* **32**, L20S07 (2005). doi: 10.1029/2005GL022648
31. J. D. Kraus, Wave polarization, in *Radio Astronomy*, 116–125 (McGraw-Hill, New York, 1966).
32. B. Cecconi et al., Goniopolarimetric study of the revolution 29 perikrone using the Cassini Radio and Plasma Wave Science instrument high-frequency radio receiver. *J. Geophys. Res.* **114**, A03215 (2009). doi: 10.1029/2008JA013830
33. L. Lamy, P. Zarka, B. Cecconi, S. Hess, R. Prangé, Modeling of Saturn kilometric radiation arcs and equatorial shadow zone. *J. Geophys. Res.* **113** (A10), A10213 (2008). doi: 10.1029/2008JA013464
34. R. L. Mutel, I. W. Christopher, J. S. Pickett, Cluster multispacecraft determination of AKR angular beaming. *Geophys. Res. Lett.* **37**, L07104 (2008). doi: 10.1029/2008GL033377
35. P. H. M. Galopeau, M. Y. Boudjada, An oblate beaming cone for Io-controlled Jovian decameter emission. *J. Geophys. Res.* **121**, 3120–3138 (2016). doi: 10.1002/2015JA021038
36. D. B. Melrose, G. A. Dulk, On the elliptical polarization of Jupiter's decametric radio emission. *Astron. Astrophys.* **249**, 250–257 (1991).
37. G. J. Hunt et al., Field-aligned currents in Saturn's magnetosphere: Observations from the F-ring orbits. *J. Geophys. Res.* **45**, 4692–4700 (2018). doi: 10.1029/2018GL077925
38. P. Louarn et al., Trapped electrons as a free energy source for the auroral kilometric radiation. *J. Geophys. Res.* **95** (A5), 5983–5995 (1990). doi: 10.1029/JA095iA05p05983

39. R. E. Ergun et al., Electron-Cyclotron Maser Driven by Charged-Particle Acceleration from Magnetic Fieldaligned Electric Fields. *Astrophys. J.* **538**, 456–466 (2000). doi: 10.1086/309094
40. P. Louarn et al., Generation of the Jovian hectometric radiation: First lessons from Juno. *Geophys. Res. Lett.* **44**, 4439–4446 (2017). doi: 10.1002/2017GL072923
41. C. K. Louis et al., Io-Jupiter decametric arcs observed by Juno/Waves compared to ExPRES simulations. *Geophys. Res. Lett.* **44**, 9225–9232 (2017). doi: 10.1002/2017GL073036
42. L. C. Ray, M. Galand, P. A. Delamere, B. L. Fleshman, Current-voltage relation for the Saturnian system. *J. Geophys. Res. Space Phys.* **118**, 3214–3222 (2013). doi: 10.1002/jgra.50330
43. S. Knight, Parallel electric fields. *Planet. Space Sci.* **21**, 741–750 (1973). doi: 10.1016/0032-0633(73)90093-7
44. D. A. Gurnett et al., The rotation of the plasmapause-like boundary at high latitudes in Saturn's magnetosphere and its relation to the eccentric rotation of the northern and southern auroral ovals. *Geophys. Res. Lett.* **38**, L21203 (2011). doi: 10.1029/2011GL049547
45. R. Bingham et al., Laboratory astrophysics: Investigation of planetary and astrophysical maser emission. *Space Sci. Rev.* **178**, 695–713 (2013). doi: 10.1007/s11214-013-9963-z
46. P. H. M. Galopeau, P. Zarka, D. Le Quéau, Theoretical model of Saturn's kilometric radiation spectrum. *J. Geophys. Res.* **94** (A7), 8739–8755 (1989). doi: 10.1029/JA094iA07p08739

SUPPLEMENTARY MATERIALS

www.sciencemag.org/content/362/6410/eaat2027/suppl/DC1
Figs. S1 to S5
References (47–56)

Science

The low-frequency source of Saturn's kilometric radiation

L. Lamy, P. Zarka, B. Cecconi, R. Prangé, W. S. Kurth, G. Hospodarsky, A. Persoon, M. Morooka, J.-E. Wahlund and G. J. Hunt

Cassini's final phase of exploration

The Cassini spacecraft spent 13 years orbiting Saturn; as it ran low on fuel, the trajectory was changed to sample regions it had not yet visited. A series of orbits close to the rings was followed by a Grand Finale orbit, which took the spacecraft through the gap between Saturn and its rings before the spacecraft was destroyed when it entered the planet's upper atmosphere. Six papers in this issue report results from these final phases of the Cassini mission. Dougherty *et al.* measured the magnetic field close to Saturn, which implies a complex multilayer dynamo process inside the planet. Roussos *et al.* detected an additional radiation belt trapped within the rings, sustained by the radioactive decay of free neutrons. Lamy *et al.* present plasma measurements taken as Cassini flew through regions emitting kilometric radiation, connected to the planet's aurorae. Hsu *et al.* determined the composition of large, solid dust particles falling from the rings into the planet, whereas Mitchell *et al.* investigated the smaller dust nanograins and show how they interact with the planet's upper atmosphere. Finally, Waite *et al.* identified molecules in the infalling material and directly measured the composition of Saturn's atmosphere.

Science, this issue p. eaat5434, p. eaat1962, p. eaat2027, p. eaat3185, p. eaat2236, p. eaat2382

ARTICLE TOOLS	http://science.sciencemag.org/content/362/6410/eaat2027
SUPPLEMENTARY MATERIALS	http://science.sciencemag.org/content/suppl/2018/10/03/362.6410.eaat2027.DC1
RELATED CONTENT	http://science.sciencemag.org/content/sci/362/6410/44.full http://science.sciencemag.org/content/sci/362/6410/eaat5434.full http://science.sciencemag.org/content/sci/362/6410/eaat1962.full http://science.sciencemag.org/content/sci/362/6410/eaat3185.full http://science.sciencemag.org/content/sci/362/6410/eaat2236.full http://science.sciencemag.org/content/sci/362/6410/eaat2382.full
REFERENCES	This article cites 49 articles, 0 of which you can access for free http://science.sciencemag.org/content/362/6410/eaat2027#BIBL
PERMISSIONS	http://www.sciencemag.org/help/reprints-and-permissions

Use of this article is subject to the Terms of Service